A finite-element method model for a ferromanganese and silicomanganese pilot furnace

by M. Sparta[1] and V.K. Risinggård[1]

Affiliation:
[1]NORCE Norwegian Research Centre AS, Universitetsveien 19, NO-4630 Kristiansand S, Norway.

Correspondence to:
V.K. Risinggård

Email:
veri@norceresearch.no

Dates:
Received: 14 Feb. 2023
Revised: 25 Jul. 2023
Accepted: 10 Aug. 2023
Published: March 2024

How to cite:
Sparta, M. and Risinggård, V.K. 2024
A finite-element method model for a ferromanganese and silicomanganese pilot furnace.
Journal of the Southern African Institute of Mining and Metallurgy, vol. 124, no. 3. pp. 85–92

DOI ID:
http://dx.doi.org/10.17159/2411-9717/2737/2024

Synopsis

We report on the development of a finite-element method model for a pilot furnace for the production of manganese alloys. The model is a multiphysics model that addresses material flow, electrical conditions, heat transfer, and physical and chemical transformations. It is capable of studying both quasi-steady and transient states in time-dependent simulations. The model includes common charge materials and fluxes and can simulate production of both ferromanganese and silicomanganese alloys with acid and basic slags, as well as changing charge compositions. The model output provides access to the material distribution in the furnace during furnace runs, temperature profiles, current paths, energy balances, and alloy and slag production rates and compositions.

Keywords

modelling, finite-element method, pilot furnace, manganese alloys.

Introduction

Ferromanganese (FeMn) and silicomanganese (SiMn) are manganese alloys produced by carbothermic reduction of manganese oxides and quartz in a submerged-arc furnace (Olsen, Tangstad, and Lindstad, 2007). In order to gain insight into the process, a pilot-scale furnace has been developed and run at the Norwegian University of Science and Technology. The furnace is used to investigate the electrical operation, effect of raw materials, coke bed formation, and more (Tangstad *et al.*, 2001, 2017; Monsen, Tangstad, and Midtgaard, 2004; Monsen *et al.*, 2007; Eidem *et al.*, 2010; Ringdalen and Tangstad, 2013).

To complement the experimental work, we have developed a comprehensive model for a pilot-scale silicomanganese furnace that takes into account the material flow, process chemistry, and electrical and thermal conditions of the furnace (Sparta *et al.*, 2021). The original model assumed a simplified charge consisting of pure carbon and silicon and manganese oxides, giving total of seven condensed species [MnO(s), MnO(l), Mn(l), SiO_2(s), SiO_2(l), Si(l), and C(s)], as well as CO(g). In this contribution we report on the expansion of the model to address both ferromanganese and silicomanganese alloys in the presence of fluxes and spectator oxides. The original model has been expanded to a total of 18 species by including Fe_2O_3(s), Fe(s), Fe(l), CaO(s), CaO(l), MgO(s), MgO(l), Al_2O_3(s), Al_2O_3(l). and CO_2(g).

Model description

This iteration of the model (FeSiMn) builds on the previous SiMn model described in Sparta *et al.* (2021). This section provides a brief overview of the original model, with particular emphasis on modifications and amendments introduced in the current version. The model is implemented using the finite-element method (FEM) in COMSOL Multiphysics (COMSOL Inc., 2022). FEM provides an accurate representation of curved surfaces and natural handling of gradient boundary conditions (Zienkiewicz and Morgan, 2006) and the multiphysics capability of the software platform is fully exploited. However, the same implementation could be achieved with other methods for representing and evaluating partial differential equations.

The cylindrical symmetry of the experimental equipment is exploited to reduce the computational cost of the model by using the two-dimensional axisymmetric interface. The furnace geometry is shown in Figure 1. For the purposes of the FEM model, the furnace consists of five domains: The top and bottom electrodes (A, C) are made of solid graphite, and are responsible for carrying the electric current into and out of the charge mix (B). The charge consists of manganese ore, quartz, coke, and fluxes. The charge and

the electrodes are contained in two structural and insulating layers made from alumina refractory bricks (D) and silica sand (E).

The dependent variables of the FEM model are: the electrical potential in the electrodes and the charge (A, B, and C); the temperature (all domains); the velocity fields of the solids, slag, and alloy phases (B); and the concentrations of all solid and liquid species (B). Furthermore, the model tracks all the material inputs and outputs for the solid, liquid, and gas phases.

Figure 2 indicates the major couplings and interactions in the multiphysics representation. Briefly, the mixing and distribution of the chemical species is determined by the advection velocities (v). The physical and chemical transformations in turn determine the void fraction (w), which drives the material flow. The local concentrations of the charge species determine the bulk material properties such as the conductivity (σ), density (ρ), and heat capacity (C_p), which in turn determine the current distribution and ohmic heat generation (q). The local temperature (T) influences the electrical conditions through the temperature dependency of the conductivity (σ), as well as the chemistry through the reactions and transformations that absorb and release heat (ΔH).

Physical and chemical transformations

For each chemical species, the model solves an advection-diffusion equation:

$$\frac{\partial c_k}{\partial t} - \nabla \cdot D\nabla c_k + v \cdot \nabla c_k + c_k \nabla \cdot v = R_k \quad [1]$$

Here, c_k is the concentration of the chemical species k, v is the velocity component of the species (described in the next section), D is the diffusion constant for the species, and R_k is its local rate of generation. The reaction rate for each species is calculated as the sum of the rates of all the reactions that the species participates in.

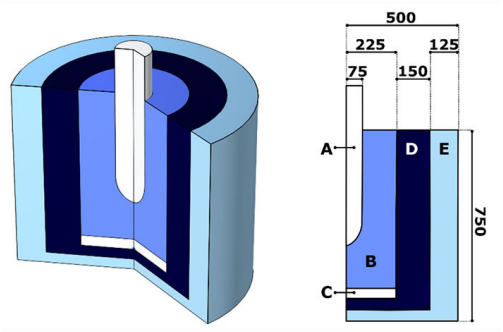

Figure 1—Visualization of the furnace proportions and its 2D axisymmetric representation. A: top electrode; B: charge; C: bottom electrode; D: alumina refractory; E: silica sand. Dimensions are given in millimetres

The current iteration of the model includes ten physical and chemical transformations. Reactions (1)–(5) below were already present in the previous version and include the melting of MnO(s) and SiO_2(s) (reactions 1 and 2), carbothermic reduction of MnO(l) and SiO_2(l) (reactions 3 and 4), and the Mn–Si exchange reaction (reaction 5). The current version also includes the solid-state reduction of iron oxide by CO gas (reaction 6), the melting of metallic iron (reaction 7), and the dissolution of fluxes and inert oxides in the slag phase (reactions 8–10).

$$\text{Reaction 1: MnO(s)} \rightarrow \text{MnO(l)} \quad [2]$$

$$\text{Reaction 2: } SiO_2\text{(s)} \rightarrow SiO_2\text{(l)} \quad [3]$$

$$\text{Reaction 3: MnO(l) + C(s)} \rightarrow \text{Mn(l) + CO(g)} \quad [4]$$

$$\text{Reaction 4: } SiO_2\text{(l) + C(s)} \rightarrow \text{Si(l) + 2CO(g)} \quad [5]$$

$$\text{Reaction 5: Si(l) + 2 MnO(l)} \rightarrow SiO_2\text{(l) + 2 Mn(l)} \quad [6]$$

$$\text{Reaction 6: } Fe_2O_3\text{(s) + 3CO(g)} \rightarrow \text{2 Fe(s) + 3 } CO_2\text{(g)} \quad [7]$$

$$\text{Reaction 7: Fe(s)} \rightarrow \text{Fe(l)} \quad [8]$$

$$\text{Reaction 8: CaO(s)} \rightarrow \text{CaO(l)} \quad [9]$$

$$\text{Reaction 9: MgO(s)} \rightarrow \text{MgO(l)} \quad [10]$$

$$\text{Reaction 10: } Al_2O_3\text{(s)} \rightarrow Al_2O_3\text{ (l)} \quad [11]$$

The reduction reactions are assumed to follow first-order rate laws (Table I) with an Arrhenius-type temperature dependence.

The activation energies are set to 200 and 250 kJ/mol for MnO and SiO_2, respectively (Canaguier and Tangstad, 2020), and 60 kJ/mol for Fe_2O_3 (Ostrovski *et al.*, 2002).

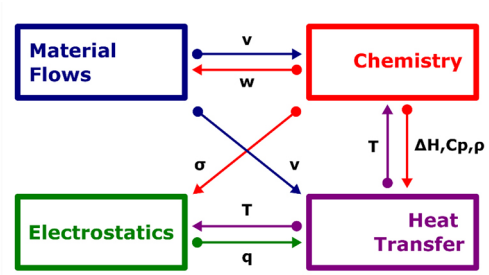

Figure 2—Modules and interactions. The functionality of the model can be understood in terms of four modules: material flows, chemistry, electrostatics, and heat transfer (adapted from Sparta *et al.* (2021)

Table I

Kinetics and enthalpies of major reactions

Reaction	Equation	k	Ea (kJ/mol)	ΔH (kJ/mol)
3	$B \cdot k \cdot \exp\left(-\frac{E_a}{T \cdot R}\right) \cdot c_{MnO(l)} \cdot (c_C > 0)$	$1 \cdot 10^3$/s	200	247
4	$k \cdot \exp\left(-\frac{E_a}{T \cdot R}\right) \cdot c_{SiO2(l)} \cdot (c_C > 0)$	$5 \cdot 10^3$/s	250	700
5	$k \cdot c_{Si(l)} \cdot c_{MnO(l)}$	$1 \cdot 10^{-5}$		−200
6	$k \cdot \exp\left(-\frac{E_a}{T \cdot R}\right) \cdot c_{Fe2O3(s)}$	1/s	60	−53

We note that from an energy balance perspective, the contributions from reactions 3 and 4 account for more than 90% of the total enthalpy of reactions. Kinetic prefactors have been selected to match average results from experimental runs on the pilot furnace.

Furthermore, the model is making use of the concept of basicity. In this work basicity refers to the ratio (CaO+MgO)/(SiO_2+ Al_2O_3) calculated on a mass basis for the tapped slag.(Olsen, Tangstad, and Lindstad, 2007) The basicity affects the following properties of the model.

- Slag liquidus temperature. The temperature at which the oxides melt into the slag phase depends on the basicity of the system (Liao, *et al.*, 2023). The liquidus temperature profile as a function of the basicity of the slags used in this work is shown in Figure 3.
- Slag fluidity. High-basicity slags are less viscous (Tangstad *et al.*, 2021). This is pragmatically included in the model by increasing the velocity at which the slag trickles through the charge by up to 30% as a function of the basicity of the slags.
- Slag reactivity. The MnO activity increases in basic slags (Tangstad *et al.*, 2021). This effect is implemented in the model by increasing the rate constants of reactions 3 and 5 by up to 50% in high-basicity slags (*B* factor in Table I).

Note that these are pragmatic and effective dependencies on the basicity, which can be further improved by using more accurate estimations or coupling with more advanced methods

Material flows

The model takes three different approaches to calculating the advection velocity *v*, depending on whether the species in question is in the solid, liquid, or gas phase.

Advection-diffusion equations are used for tracking all the species in the condensed phases. For the solid phases, an advection velocity field for the flow of granular material is calculated using the dissipative Coulomb model. This model is based on the Navier-Stokes equations for incompressible flow:

$$\nabla \cdot \vec{v} = 0 \quad [12]$$

$$\rho\left(\frac{\partial \vec{v}}{\partial t} + (\vec{v}\cdot\nabla)\vec{v}\right) = -\nabla p + \eta\nabla^2\vec{v} \quad [13]$$

Here, $\vec{v}$ is the granular velocity, p is the pressure, ρ is the medium density, and η is the medium viscosity. The local density of the effective medium is calculated from the composition of the charge or coke bed as $\rho = \Sigma_k \chi_k \rho_k$, where ρ_k is the density of species k and χ_k is its volume fraction (Artoni, *et al.*, 2008). The flow is driven by the formation of voids in the lower part of the furnace as the solid material t reacts to form liquid metal and slag. The liquid material subsequently trickles down through the granular coke bed. For the liquid phases, precomputed velocity templates are used in the advection-diffusion equations. The slag velocity is dependent on the basicity, as described in the previous section, whereas the alloy velocity is taken to be independent of the alloy composition.

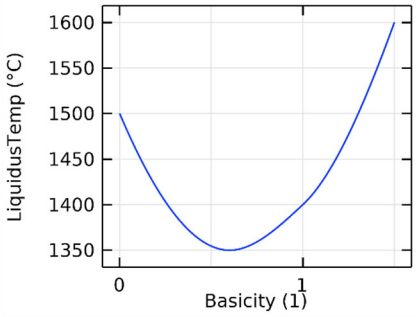

Figure 3—Effect of basicity. The liquidus temperature decreases for higher basicity

The gas flow is not addressed in the current version of the model. The fluxes of CO and CO_2 escaping at the top of the furnace are calculated as integrals over the gas-producing reactions in the charge.

Electrostatics

The direct current (DC) approximation is used to determine the electrostatic properties of the system. This approximation is satisfactory for small furnaces with a power factor close to unity (Eidem *et al.*, 2010; Halvorsen, Olsen, and Fromreide, 2016; Fromreide *et al.*, 2021).

In the case of power distribution in industrial-scale furnaces, DC simulations and linear combination of DC solutions can be used as a fair approximation to a full AC description.(Halvorsen, Olsen, and Fromreide, 2016; Tesfahunegn *et al.*, 2020; Fromreide *et al.*, 2021) The electrostatic potential V is obtained by solving the Poission equation

$$\nabla^2 V = 0 \quad [14]$$

in domains A, B, and C in Figure 1. The electric field $\vec{E}$ and the current density $\vec{J}$ are obtained from the electrostatic potential by the constitutive relationships $\vec{E} = -\nabla V$ and $\vec{J} = \sigma\vec{E}$. A constant power of 150 kW (Tangstad *et al.*, 2001, 2017; Monsen, Tangstad, and Midtgaard, 2004; Monsen *et al.*, 2007; Eidem, Tangstad, and Bakken, 2009; Eidem *et al.*, 2010) is maintained by adding a global constraint to the system. The conductivity of the electrodes is constant and set to 80 kS/m (Haynes, Lide, and Bruno, 2017), whereas the conductivity of the charge depends on the local composition. The bulk conductivity of the charge is calculated as the sum of the conductivities of each component weighted by volume fraction,

$$\sigma = \sigma_C(T)v_C + \sum_i^{Fe,Si,Mn} \sigma_i v_i \quad [15]$$

The material conductivities for the reduced species [Fe(s,l), Si(l), Mn(l)] are set to 10 kS/m. The material conductivity for carbon is dependent on temperature, increasing linearly from 10 to 400 S/m in the range 800–1600°C, with the extreme values acting as cut-offs for lower and higher temperatures (Surup *et al.*, 2020). The oxides do not contribute to the conductivity.

Heat transfer

The local temperature is determined by solving the heat equation:

$$\rho c_p\left(\frac{\partial T}{\partial t} + \vec{v}\cdot\nabla T\right) - \nabla\cdot k\nabla T = Q \quad [16]$$

Here, T is temperature, ρ is the medium density, c_p is the medium heat capacity, $\vec{v}$ is the advection velocity, k is the thermal condutivity, and Q is the local heating

$$Q = \vec{J}\cdot\vec{E} + \sum_{\text{Reaction}} \Delta H \quad [17]$$

comprising the resistive term ($\vec{J}$ is the current density, $\vec{E}$ is the electric field), and total enthalpy of reactions. In the charge, the local density and heat capacity are calculated from the local charge composition based on a weighted average, similar to that used for the electrical conductivity in Equation [15] . The thermal

conductivity is taken to be independent of the charge composition but takes into account radiative heat transport in pores and voids. A model similar to the one described by Schotte (1960) is used, but with an additional contribution from heat conduction through the particle contact points added in series with the radiative contribution. The particle thermal conductivity is taken to be 30 W/m·K (the value compensates for the lack of the convective effects of the CO/CO_2 counterflow), the contact point effective thermal conductivity is taken to be 2 W/m·K, the particle diameter is set to 30 mm, and the emissivity to 0.9. This results in a thermal diffusivity that is somewhat higher than experimentally measured bulk thermal diffusivities for common manganese ores (Ksiazek et al., 2013), which is to be expected given the contribution from the higher conductivity carbon material.

Simulation modes

The FEM model solves for the time evolution of the system. Tapping and charging occur in a continuous way. Liquid species that reach the level of the bottom electrodes are removed from the simulation and accounted as tapped flow. A constant charge level is maintained by continually adding an amount of charge corresponding to the volume of material consumed in the hearth of the furnace. The composition of the incoming charge is specified by the user, and can be set to be:

- **Constant** for the duration of the simulation. This mode can be used, for example, to simulate a start-up stage when the internal temperature is increasing, or during over-coking or under-coking (periods in which the charge contains more or less carbon than needed).
- **Switching** from an initial to a final set of concentrations at a prescribed time. For example, this can be used to study a transient state. In the examples below, this mode will be used to investigate what happens when the charge switches from a composition rich in iron and acid oxides to a silicomanganese one rich in basic oxides.

For a suitable amount of carbon in the charge mix, the constant charge mode will eventually reach a quasi-steady state. The depth of the coke bed in this steady state depends on the carbon balance of the charge. Insufficient carbon coverage will lead to a shallow coke bed and excessive slag production. Excessive amounts of carbon will give rise to an ever-deepening coke bed that eventually fills the furnace.

To more closely simulate industrial operation, an additional control is implemented for the carbon content in the charge mix. For either mode, the amount of carbon in the mass flux that is added to the system can be adaptive, meaning that the amount added matches the amount of carbon consumed in the reactions and escaping as CO/CO_2. This simulates the ideal situation, in which an exact carbon coverage is maintained. If the initial conditions are relatively close to the equilibrated solution, adaptive coking leads to a quasi-steady state solution determined by the input power and relative ratios of the metal oxides in the charge. Adaptive coking will be demonstrated in the second simulation example below.

Simulation examples

Quasi-steady state

The first simulation presented aims at reaching a steady state. For this example, the input power is set to 150 kW and the charge composition is as specified in Table II.

Table II

Composition of the charge for a 20 kg batch

Species	Charge I	
	kg	wt%
MnO	9.79	48.9
SiO_2	4.82	24.1
Fe_2O_3	1.12	5.6
Al_2O_3	2.16	10.8
CaO	0.25	1.25
MgO	0.13	0.67
Carbon	1.73	8.7

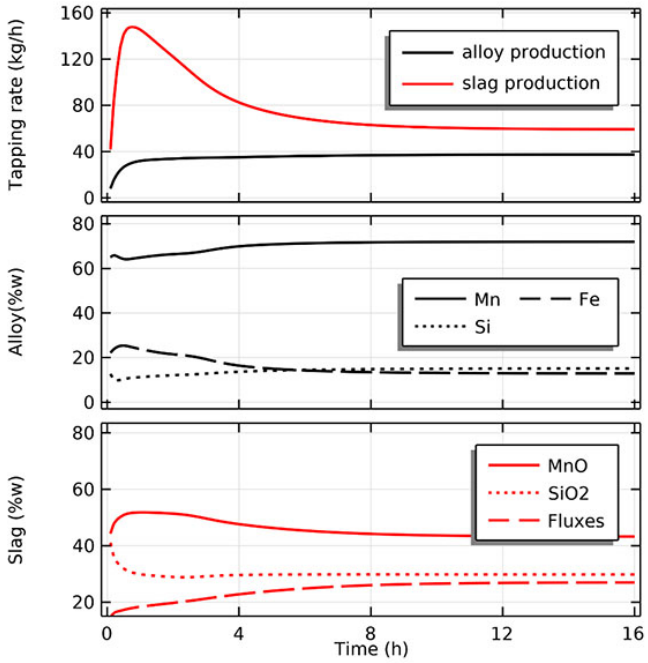

Figure 4—Top: Production rates of alloy and slag (kg/h) during a 16-hour simulation run. Centre: Composition of the alloy (wt%). Bottom: Composition of the slag

The initial condition is a homogenous charge at 800°C with the composition specified in Table II. The production profiles of slag and alloy and their compositions are reported in Figure 4. In the early stage the furnace is cold, and most of the oxides dissolve in the slag phase and leave the system without reacting any further. This means that, in the early stage of the run, the furnace is fed with an excess of carbon that accumulates in a coke bed between the electrodes. As the furnace warms up and enough energy is available, the slag percolating through the carbon-rich zone undergoes carbothermic reduction and the carbon consumption increases until a balance is reached.

After 16 hours, the furnace reaches a quasi-steady state with an alloy and slag production of approximately 38 and 59 kg/h, respectively. Considering this hourly production and the input power of 150 kW, the energy consumption is 3.9 kWh/kg of alloy, a value in line with experimental values (Monsen, Tangstad, and Midtgaard, 2004; Monsen *et al.*, 2007; Eidem, Tangstad, and Bakken, 2009; Eidem *et al.*, 2010).

Regarding the composition of the tapped material, the alloy has a relatively high iron content in the early stages of the run as the direct gas-solid reduction of iron oxide starts occurring at relatively low temperatures. As the system reaches equilibrium

the iron content stabilizes and the alloy has a final composition of 72 wt% Mn, 15% Si, and 13% Fe. For the charge mix used in this simulation, the the slag at equilibrium contains 43 wt% MnO, 30% SiO_2, and 27% fluxes. As can be seen in Figure 4, this simulation run demonstrates that the model can reach a stable state with a carbon consumption matching the incoming charge, provided that reasonable values for the energy input and charge recipe are supplied.

Figure 5 shows the conditions in the furnace at the end of the simulation. Directly below the top electrode one finds the hot zone, with temperatures exceeding 2000°C (left panel). The entire coke bed has a temperature exceeding 1400°C. The coke bed can be visualized by plotting the volume fraction of carbon in the furnace (middle panel). The boundary of the coke bed is located between the 1600 and 1800°C isotherms. The divergence of the velocity of the granular material is shown in the right panel. The divergence $\mathrm{div}\vec{v}$ is calculated as $\mathrm{div}\vec{v} = \nabla \cdot \vec{v}$. The negative divergence indicates that granular material is converging on the interface between the charge and the coke bed. In other words, in this region solid material is consumed by melting and by chemical reactions.

The species distribution for the triad MnO(s), MnO(l), and Mn(l) is shown in Figure 6. MnO(s) is the only species present during the descent of the charge from the top of the furnace to the top of the coke bed. MnO(l) forms when the charge has passed the 1600°C isotherm, and Mn(l) forms by carbothermic reduction of MnO(l) in the coke bed.

Owing to the relatively fast percolation of the slag, although the charge contains 30 wt% MnO, the liquid MnO never exceeds approximately 0.6 wt%. The rate of carbothermic reduction of MnO increases with temperature, leading to the profile seen for Mn(l). The distribution of Si-containing species follows the same pattern. Results from the excavation of the pilot furnace are in line with the simulations, *i.e.* MnO is scarce in the column directly below the electrode and is mostly found in the periphery of the furnace, and Si is mostly concentrated directly below the top electrode (Tangstad *et al.*, 2001).

The profiles for the iron species are markedly different to those for manganese and silicon, as shown in Figure 7. Iron oxides are reduced in the solid state by the CO(g) passing upward through the solid charge. The charge in the proximity of the electrode is warmer (see Figure 5), consequently unreacted Fe_2O_3 can be found deeper in the furnace at the periphery than at the centre. Solid metallic iron exists between the 800 and 1800°C isotherms above the top of the coke bed. The iron starts to melt as it reaches the top of the coke bed and enters the liquid alloy phase. It should be noted that the kinetics of the solid-gas reaction ultimately depend on the CO diffusion in the solid particles – this in turn depends on the porosity and size of the particles. These dependencies are not explored in the model.

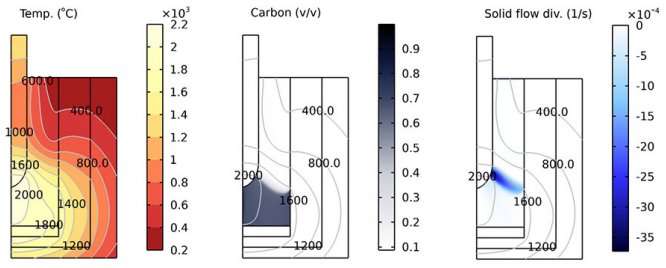

Figure 5—Left: Temperature distribution (°C) at the end of the simulation. Centre: Carbon concentration (v/v) confirms the formation of a coke bed. Right: Divergence of the solid flow (1/s). All panels show isothermal contours (°C)

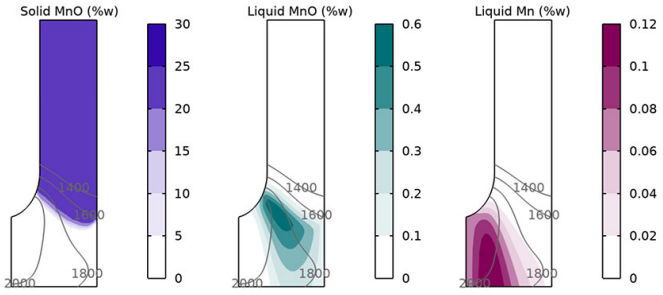

Figure 6—MnO(s), MnO(l), and Mn(l) distribution in the charge domain (wt%). Isothermal contours (°C)

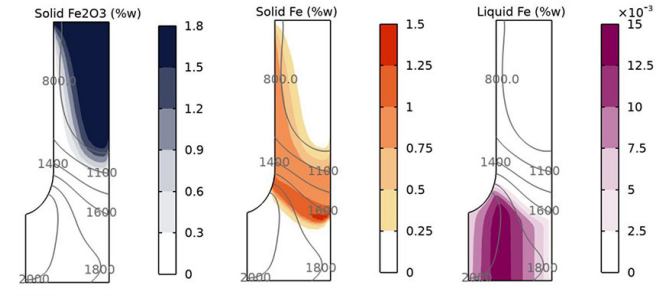

Figure 7—Fe_2O_3(s), Fe(s), and Fe(l) distributions in the charge domain (wt%). Isothermal contours (°C)

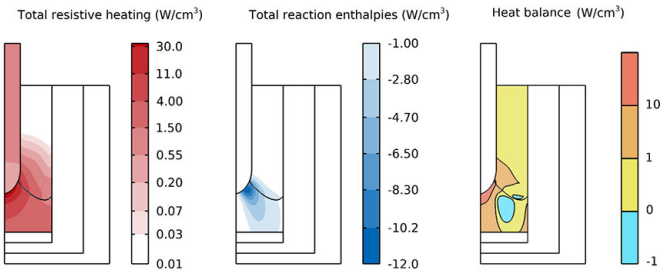

Figure 8—Total resistive heating (left), reaction enthalpies (centre), and heat balance (right) in W/cm³. The black line in the charge marks the boundary of the coke bed

Figure 8 depicts the heat balance of the system. The left panel shows the distribution of ohmic heat generated by the applied electrical current. The boundary of the coke bed (marking where carbon content exceed 50 wt%) is shown with a black line for convenience. One notices that, because of the DC approximation, there is no accumulation of current at the surface of the electrode (skin effect), and the heat generated in the electrode is distributed homogenously. In the charge, the current paths with the least resistance pass through the tip of the top electrode and spread out in the coke bed to reach the flat bottom electrode, hence the heat generation in the charge is concentrated near the tip of the top electrode. The resistance of the coke bed varies between 3 and 4 mΩ·m as a function of position, in close agreement with experimental estimates (Eidem, Tangstad, and Bakken, 2009). The total resistance of the furnace is about 10 mΩ, similar to values from experimental runs in this pilot furnace (Ringdalen and Tangstad, 2013).

The central panel in Figure 8 shows the sum of the reaction enthalpies. Overall, the reactions are endothermic, and most of the thermal energy consumed by the reactions is used in the coke bed near the tip of the top electrode. The endothermic contributions from reactions 3 and 4 (the carbothermic reduction of silicon

and manganese oxides) are the dominating terms. This correlates well with the species distribution (Figure 6) and temperature distribution (Figure 5): liquid oxides that flow the hot region near the tip of the electrode react readily and trickle downward as alloy droplets. Conversely, closer to the periphery the lower temperature results in a less efficient conversion of the slag. The total heat balance (right panel) is obtained by combining the ohmic heating with the reaction enthalpies. Here it can be seen that the resistive heating produces excess heat to maintain the reactions in the region near the electrode. Excess heat is also produced at the furnace periphery. The mid-section of the coke bed is the only region with a negative heat balance. However, note that as the simulation has reached a quasi-steady state, the system is in thermal equilibrium. All the excess heat produced in the core of the furnace and at the furnace periphery is used to either (1) compensate the deficit in the middle of the coke bed, (2) heat the incoming charge, or (3) compensate the heat loss at the furnace surface.

Finally, in Figure 9 the production and consumption of nine major species is show as the rates of reaction (mol/m^{3}s). Examination of the figure confirms that the dissolution of the species and the reduction reactions occur in different zones.

Transient state

The second simulation aims at studying the conditions in the furnace when changing the charge recipe from a composition rich in iron and acidic oxides (Table II) to a silicomanganese charge rich in basic oxides (Table III). The initial condition corresponds to the quasi-steady state reached at the end of the simulation presented in the previous section. The simulation spans 6 hours and at t =1 h the charge switches from the initial recipe to the final composition. Furthermore, an adaptive carbon coverage is used, meaning that the incoming flux of carbon matches the amount consumed by the carbothermic reduction reactions.

The evolution of the product in the 6-hour run is shown in Figure 10. Although the composition of the charge changes at t = 1 h, (marked in the plot by a blue vertical dashed line), the composition of the products tapped at the bottom of the furnace remains constant up to about t = 1.8 h, since the new charge has to descend and reach the core of the furnace before impacting the system. Once this occurs, the furnace transitions into a new regime within 1–2 hours. Production of both alloy and slag decreases, and the iron content in the alloy drops. The final composition of the alloy is approximately 80 wt% manganese and 20 wt% silicon. The silicon content in the alloy is comparable to experimental runs in this furnace (Ringdalen and Tangstad, 2013) and in line with that of industrial alloys (Olsen, Tangstad, and Lindstad, 2007). The content of fluxes in the slag remains quite constant (28 wt%). The content of

Table III

Composition of the charge for a 20 kg batch: /transient state

Species	Charge	
	kg	wt%
MnO	9.68	48.4
SiO_2	5.95	29.8
Fe_2O_3	0.0	0.0
Al_2O_3	0.56	2.8
CaO	1.23	6.2
MgO	0.48	2.4
Carbon[a]	2.09	10.4

[a]Carbon content varies with consumption in the core.

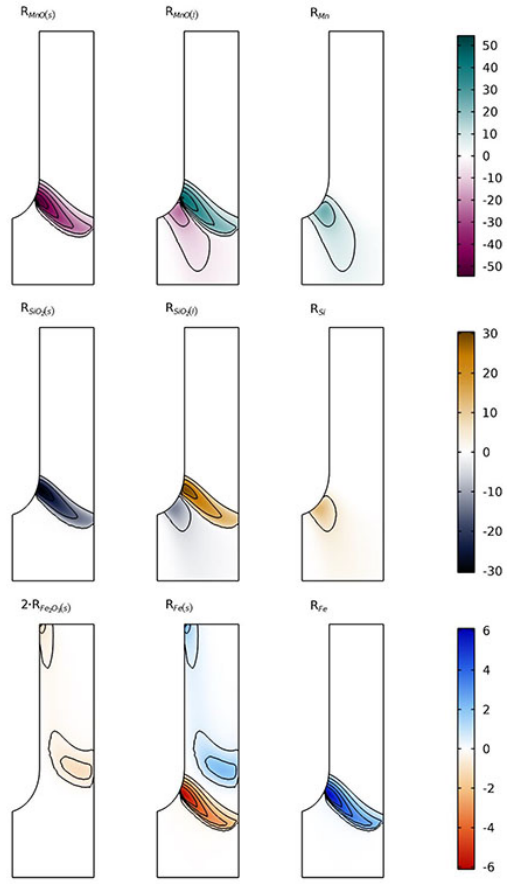

Figure 9—Production and consumption of nine major species (mol/m^{3}s)

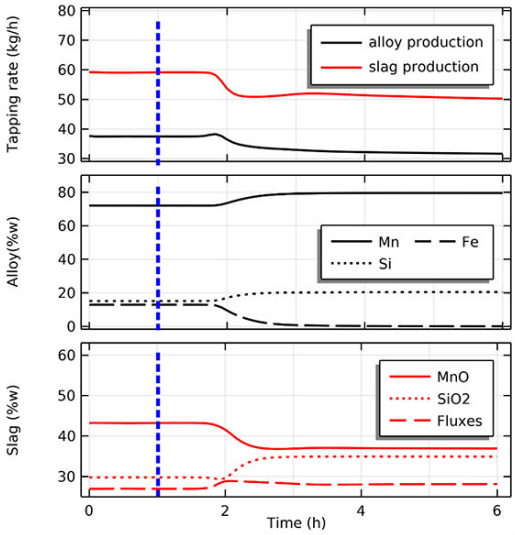

Figure 10—Top: Production of alloy and slug (kg/h) during a 6-hour simulation run with switching of the charge composition after 1 h (blue vertical dashed line). Centre: Composition of the alloy (wt%). Bottom: Composition of the slag

SiO_2 increases to 35 wt% and, as expected, the MnO content of the slag decreases with increasing basicity, ending up at 37 wt%.

It is interesting to study the different temperature distributions in the furnace at the two quasi-steady states, as shown in Figure 11. One can observe three major differences.

1. The top part of the electrode is much colder; this is a direct effect of the lower conductivity of the charge due to the lack

of ferrous material. The total resistance of the systems is therefore increased, and hence a lower current is needed to reach 150 kW of power.

2. A much higher temperature is found at the tip of the top electrode. This is because although the total current is lower, current accumulates at the tip of the top electrode and increases the power density in that area.
3. The charge in the middle of the furnace is significantly colder, owing to the reduced amount of heat in the area (see point 2) and less heat being transported away from the core. The latter phenomenon is partly due to the higher activity of MnO in the basic slag and a higher reactivity near the hot zone.

Interestingly, the furnace at the beginning of the simulation would appear warmer than at the end, whereas the situation is reversed in the core.

In conclusion, the final quasi-steady state shows larger temperature gradients in the charge approaching the coke bed. This, and the higher activity of MnO in the basic slag, effectively reduces the reaction volume and places it closer to the tip of the electrode, as shown in Figure 12. Despite this pronounced peak in th Mn production rate, the total Mn production is greater for charge I (27 kg/h) than for charge II (25.1 kg/h).

Summary

We have expanded our previous model of a pilot-scale silicomanganese furnace to allow for the study of the ferromanganese process and to investigate the effect of different fluxes.

In total, the movement of 18 chemical species is tracked: two species in the gas phase – CO(g) and CO_2(g) – and 16 in the condensed phases – MnO(s), MnO(l), Mn(l), SiO_2(s), SiO_2(l), Si(l), C(s), Fe_2O_3(s), Fe(s), Fe(l), CaO(s), CaO(l), MgO(s), MgO(l), Al_2O_3(s), and Al_2O_3(l).

The model uses the quaternary basicity ratio (CaO+MgO)/(SiO_2+ Al_2O_3) calculated on a mass basis, to encode experimental observations into the controlling equations for the material flows, process chemistry, and electrical and thermal conditions in the furnace.

As for the previous iteration, the model predictions of process parameters such as slag and alloy production rates and compositions are in agreement with experimental values (Ringdalen and Solheim, 2018). In addition, the model complements the information from experiments with insights like the internal temperature distribution and the concentrations of different chemical species in the hearth during the production run.

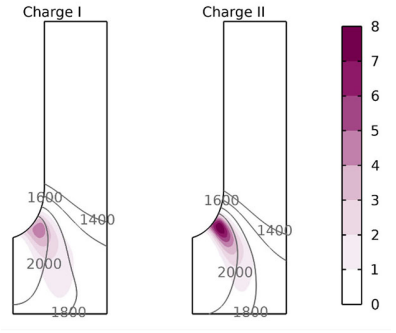

Figure 12—Production of Mn (g/cm³ h) at the beginning and end of the simulation

Acknowledgements

The support from SFI-Metal production (project no. 237738), a Norwegian Centre for Research-Based Innovation, is acknowledged.

Credits

MS: Conceptualization, Methodology, Investigation, Writing - Original draft preparation. VKR: Methodology, Validation, Writing-Reviewing and Editing.

References

Artoni, R., Santomaso, A., and Canu, P. 2008. A dissipative Coulomb model for dense granular flows. *AIP Conference Proceedings*, vol. 1027. p. 941. https://doi.org/10/c53425

Canaguier, V. and Tangstad, M. 2020. Kinetics of slag reduction in silicomanganese production. *Metallurgical and Materials Transactions B*, vol. 51, no. 3. pp. 953–962. https://doi.org/10.1007/s11663-020-01801-3

COMSOL Inc. 2022 COMSOL multiphysics. https://www.comsol.com/

Eidem, P.A., Tangstad, M., and Bakken, J.A. 2009. Electrical conditions of a coke bed in SiMn production. *Canadian Metallurgical Quarterly*, vol. 48. p. 355. https://doi.org/10/ghcz4s

Eidem, P.A., Tangstad, M., Bakken, J.A., and Ishak, R. 2010. Influence of coke particle size on the electrical resistivity of coke beds. *Proceeding of the Twelfth International Ferroalloys Congress, INFACON XII*, Helsinki, Finland. Outotec Oyj, Finland. pp. 349-358. https://www.pyrometallurgy.co.za/InfaconXII/349-Eidem.pdf

Fromreide, M., Gómez, D., Halvorsen, S.A., Herland, E.V., and Salgado, P. 2021. Reduced 2D/1D mathematical models for analyzing inductive effects in submerged arc furnaces. *Applied Mathematical Modelling*, vol. 98. pp. 59–70. https://doi.org/10.1016/j.apm.2021.04.034

Halvorsen, S.A., Olsen, H.A.H., and Fromreide, M. 2016. An efficient simulation method for current and power distribution in 3-phase electrical smelting furnaces. *IFAC-PapersOnLine*, vol. 49, no. 20. pp. 167–172. https://doi.org/10/gf9hgp

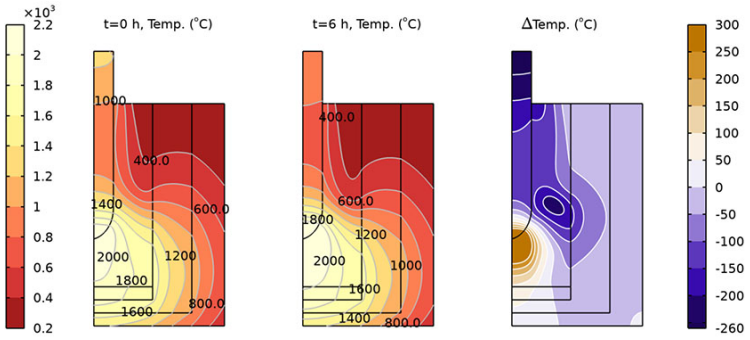

Figure 11—Temperature at the beginning (left, FeMn acid charge) and end of the 6-hour simulation (centre, SiMn basic charge), and temperature difference between the two states (right)

Haynes, W.M., Lide, D.R., and Bruno, T.J. 2017. CRC Handbook of Chemistry and Physics. 97th edn. CRC Press.

Ksiazek, M., Manik, T., Tangstad, M., and Ringdalen, E. 2013. The thermal diffusivity of raw materials for ferromanganese production. *Proceeding of the Thirteenth International Ferroalloys Congress, INFACON XIII*, Almaty, Kazakhstan, pp. 127-136. https://www.pyrometallurgy.co.za/InfaconXIII/0127-Ksiazek.pdf

Liao, J., Qing, G., and Zhao, B. 2023. Phase equilibrium studies in the CaO–SiO_2–Al_2O_3–MgO system with MgO/CaO ratio of 0.2. *Metallurgical and Materials Transactions B*, vol. 54, no. 2. pp. 793–806. https://doi.org/10.1007/s11663-023-02726-3

Monsen, B., Tangstad, M., and Midtgaard, H. 2004. Use of charcoal in silicomanganese production. *Proceeding of the Tenth International Ferroalloys Congress, INFACON X*, Cape Town, South Africa. pp. 392–404. https://www.pyrometallurgy.co.za/InfaconX/009.pdf

Monsen, B., Tangstad, M., Solheim, I., Syvertsen, M., Ishak, R., and Midtgaard, H. 2007. Charcoal for manganese alloy production. *Proceeding of the Eleventh International Ferroalloys Congress, INFACON XI*, New Delhi, India, pp. 297-310. https://www.pyrometallurgy.co.za/InfaconXI/297-Monsen.pdf

Olsen, S.E., Tangstad, M., and Lindstad, T. 2007. Production of Manganese Ferroalloys. Tapir Akademisk Forlag, Trondheim, Norway.

Ostrovski, O., Olsen, S.E., Tangstad, M., and Yastreboff, M. 2002. Kinetic modelling of MnO reduction from manganese ore. *Canadian Metallurgical Quarterly*, vol. 41, no. 3. pp. 309–318. https://doi.org/10.1179/cmq.2002.41.3.309

Ringdalen, E. and Solheim, I. 2018. Study of SiMn process in a pilot furnace. *Proceeding of the Fifteenth International Ferroalloys Congress, INFACON XV*, Cape Town, South Africa. Southern African Institute of Mining and Metallurgy, Johannesburg.

Ringdalen, E. and Tangstad, M. 2013. Study of SiMn production in pilot scale experiments – comparing Carajas sinter and Assmang ore. *Proceeding of the Thirteenth International Ferroalloys Congress, INFACON XIII*, Almaty, Kazakhstan. pp. 195-205. https://www.pyrometallurgy.co.za/InfaconXIII/0195-Ringdalen.pdf

Schotte, W. 1960. Thermal conductivity of packed beds. *AIChE Journal*, vol. 6. p. 63. https://doi.org/10/b3dgz9

Sparta, M., Risinggård, V.K., Einarsrud, K.E., and Halvorsen, S.A. 2021. An overall furnace model for the silicomanganese process. *Journal of the Minerals, Metals & Materials Society*, vol. 73, no. 9. pp. 2672–2681. https://doi.org/10.1007/s11837-021-04791-y

Surup, G.R., Pedersen, T.A., Chaldien, A., Beukes, J.P., and Tangstad, M. 2020. Electrical resistivity of carbonaceous bed material at high temperature. *Processes*, vol. 8, no. 8. p. 933. https://doi.org/10.3390/pr8080933

Tangstad, M., Bublik, S., Haghdani, S., Einarsrud, K.E., and Tang, K. 2021. Slag properties in the primary production process of Mn-ferroalloys. *Metallurgical and Materials Transactions B*, vol. 52, no. 6. pp. 3688–3707. https://doi.org/10.1007/s11663-021-02347-8

Tangstad, M., Heiland, B., Olsen, S.E., and Tronstad, R. 2001. SiMn production in a 150 kVA pilot scale furnace. *Proceeding of the Ninth International Ferroalloys Congress, INFACON IX*, Quebec City, Canada. pp. 401-406. https://www.pyro.co.za/InfaconIX/401-Tangstad.pdf

Tangstad, M., Ringdalen, E., Manilla, E., and Davila, D. 2017. Pilot scale production of manganese ferroalloys using heat-treated Mn-nodules. *Journal of the Minerals, Metals & Materials Society*, vol. 69. p. 358. https://doi.org/10/f9pvxj

Tesfahunegn, Y.A., Magnusson, T., Tangstad, M., and Saevarsdottir, G. 2020. Comparative study of AC and DC solvers based on current and power distributions in a submerged arc furnace. *Metallurgical and Materials Transactions B*, vol, 51. pp. 510–518.

Zienkiewicz, O.C. and Morgan, K. 2006. Finite Elements and Approximation. Dover, Mineola, NY. ◆